Heat dynamics in optical ring resonators

Walter Dickmann*[a,b], Lukas Max Weituschat[c], René Eisermann[b], Stephan Krenek[b], Pablo Aitor Postigo[c], Stefanie Kroker[a,b]
[a]Technische Universität Braunschweig, LENA Laboratory for Emerging Nanometrology, Langer Kamp 6, 38106 Braunschweig, Germany; [b] Physikalisch-Technische Bundesanstalt (PTB), Bundesallee 100, 38116 Braunschweig, Germany; [c] Spanish National Research Council, Instituto de Micro y Nanotecnología, IMN-CNM, CSIC (CEI UAM+CSIC) Isaac Newton, 8, E-28760 Tres Cantos, Madrid, Spain

ABSTRACT

We present an analytical model for the dynamical self-heating effect in air-cladded optical microring resonators (ORRs). The spatially and time resolved temperature field is calculated by integrating the corresponding boundary value problem of the heat equation. It turns out that the self-heating amplitude is approximately proportional to the total absorbed power and anti-proportional to the thermal conductivity of the cladding material. Further, two-photon absorption plays a major role in the heating process, even for moderate input powers, due to the strong light confinement. Heating times are determined to be in the microsecond range and may limit the response time of ORR devices. The explicit formulas for the temperature fields allow a much faster determination of heating properties compared to elaborate finite element simulations. Thus, our model is predestinated for scanning large parameter spaces.

Keywords: optical ring resonators, heat equation, absorption, two-photon absorption, temperature sensing, thermal modeling

1. INTRODUCTION

Optical microring resonators (ORRs) are circular waveguide structures with sub-wavelength thicknesses and diameters in the µm-range. High index resonator structures are embedded into low index dielectric claddings. Those devices enable a variety of biological [1,2], chemical [3,4] and physical [5,6] sensing applications with unique spatial resolution. A prominent physical application is the precise and robust measurement of temperature [7,8]. A typical configuration is the all-pass-filter [9], where light is evanescently coupled from a straight bus waveguide into the resonator ring [10]. Resonances in the ring lead to anti-resonances in the outcoupled light. As the spectral position of those resonances is shifted by temperature changes via the thermo-optical effect, probing this position gives access to the temperature of the ORR.

Refractive index pertubations, caused by optical absorption processes, lead to a superimposed resonance distortion. Created charge carriers couple to the dielectric function of the ring material by electro-optical effects such as bandgap shrinkage [11] and band filling [12]. Further, excess energies during the absorption and non-radiative recombinations insert heat into the resonator ring. Both these mechanisms lead to a superimposed resonance shift. Additionally, optical bistability effects [13], induced by the two-photon absorption (TPA) process [14], cause a strong asymmetry in the resonance shape [15] for very high intensities.

In this work, we derive analytical formulas for the self-heating effect in air-cladded ORRs. For that purpose, the heat equation with its corresponding boundary conditions and an absorption induced heat source is integrated on the ORR domain. Although not all occurring integrals can be expressed in terms of elementary functions, the explicit formulas for the spatially and time resolved temperature fields can be evaluated with substantially reduced computational costs compared to a rigorous numerical solution of the boundary value problem. Furthermore, physical dependencies manifest in a direct way here. For a comparison and verification of the analytical results, rigorous finite element simulations are performed.

Modeling Aspects in Optical Metrology VIII, edited by Bernd Bodermann
Karsten Frenner, Proc. of SPIE Vol. 11783, 1178309 · © 2021 SPIE
CCC code: 0277-786X/21/$21 · doi: 10.1117/12.2592552

2. THE ANALYTICAL SELF-HEATING MODEL

Geometry of optical ring resonators

We investigate ORRs in the all-pass-filter configuration [9], as depicted in figure 1. A high-index resonator ring of width b, height d and diameter D is evanescently coupled to a straight bus waveguide through a gap g. The waveguides are placed on a low refractive index bottom cladding, typically made of silica glass, and are covered by a top cladding. In the scope of this work, the top cladding is air. For the formulation of the boundary value problem, see section 2.2, a Cartesian coordinate system (x_1, x_2, x_3) is utilized as shown in figure 1.

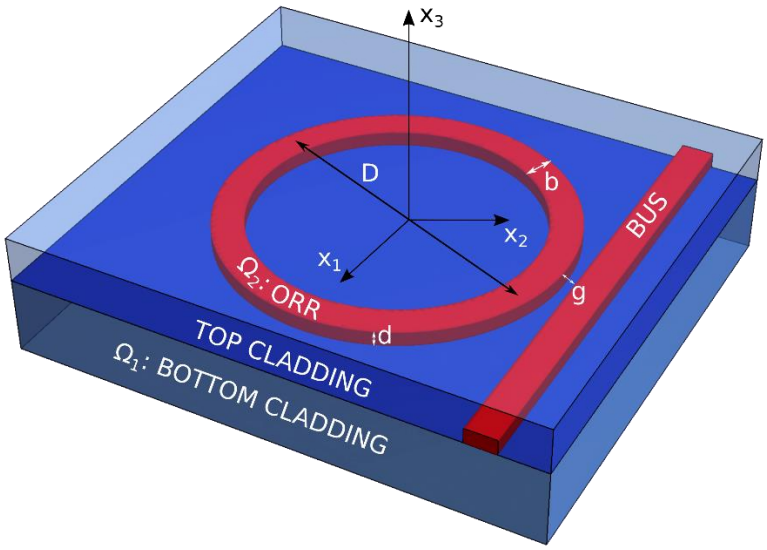

Figure 1. All-pass-filter configuration of an optical ring resonator device. The ring and bus waveguides are placed on a low refractive index bottom cladding and are covered by a top cladding.

The boundary value problem

Although photon energies far below the band gap of the resonator material are typically used, guided light in optical ring resonators gets partially absorbed. Linear absorption processes that include defect states and TPA lead to the creation of free charge carriers [15]. The resulting change in the carrier concentration directly influences the resonance conditions by electro-optical effects [11,12]. While the excess energy of the absorption process is directly transferred into heat, recombinations occur after respective lifetimes τ. In indirect semiconductor materials like crystalline silicon, nearly all recombinations are non-radiative [16]. Thus, the annihilation energy is also transferred into heat. Charge carrier lifetimes in silicon microring resonators are in the order of $\tau = 1$ ns [17], so that the time delay between absorption and heat creation is neglected here.

The following self-heating model is an extension to a previous calculation for thermal equilibrium, presented in Weituschat *et al.* [18], to the full heating dynamics. In order to formulate the boundary value problem that defines the temperature field, the following approximations are pre-determined:

(I) The bottom cladding region Ω_1 is very large and set to be equal to the lower Euclidean half-space, i.e. $\Omega_1 = \mathbb{R}^3_-$.

(II) While the bottom cladding is typically made of silica glass [19], the resonator ring consists of crystalline materials such as silicon. Thus, the thermal diffusivity a in the former is much smaller than in the latter, i.e. $a_1 \ll a_2$ (see table 1).

(III) A critical self-heating is expected exclusively on resonance due to the high resonator finesse. Here, the intensity distribution $I(\boldsymbol{x}, t)$ in the ring is overall much higher than in the bus waveguide, which is consequently neglected. Further, I is assumed to be spatially homogeneous.

(IV) We investigate air-cladded devices, making the heat flow into the top cladding negligible.

In the whole device Ω, the temperature field $T(\boldsymbol{x}, t)$ satisfies the heat equation

$$\partial_t T(\boldsymbol{x}, t) - a\, \boldsymbol{\nabla}^2 T(\boldsymbol{x}, t) = f(\boldsymbol{x}, t) \text{ in } \Omega, \tag{1}$$

where f is the local volumetric heat source [20]. According to approximation (IV), the whole inserted heat into the ring is transferred to the bottom cladding via the interface in between. Further, the heating time is predominantly determined by the cladding due its much lower thermal diffusivity, see table 1. Due to the very thin waveguide width compared to the ring diameter ($b \ll D$, see table 1), the heat source f_1 utilized for the heating calculation in the bottom cladding is approximated as a delta distributed ring apart from the interface:

$$f_1(\boldsymbol{x}) = bd\,\frac{\alpha I + \beta I^2}{\rho_1 c_{\mathrm{m1}}}\,\delta\left[\varrho - \frac{D}{2}\right]\delta[x_3], \tag{2}$$

with the constant light intensity in the ring I, the linear attenuation coefficient α, the TPA coefficient β, the cladding mass density ρ_1, the cladding heat capacity c_{m1} and cylindrical coordinates (ϱ, φ, x_3). Both linear absorption processes from defect states and TPA are considered here, leading to $\alpha I + \beta I^2$ for the absorbed power density [21]. A very large bottom cladding $\mathbb{R}^3_$, surrounded by air with negligible heat release, fulfills insulating boundary conditions (BCs) [22]. That leads to the Neumann problem:

$$\begin{aligned} &\partial_t T_1(\boldsymbol{x}, t) - a_1\, \boldsymbol{\nabla}^2 T_1(\boldsymbol{x}, t) = f_1(\boldsymbol{x}) \text{ in } \Omega_1 \backslash \left\{\boldsymbol{x} | \varrho \in \left[\frac{D}{2} - \frac{b}{2}, \frac{D}{2} + \frac{b}{2}\right]\right\} \text{ and} \\ &\boldsymbol{\nabla} T_1(\boldsymbol{x}) = \boldsymbol{0} \text{ on } \partial\Omega_1 \backslash \left\{\boldsymbol{x} | \varrho \in \left[\frac{D}{2} - \frac{b}{2}, \frac{D}{2} + \frac{b}{2}\right]\right\}, \end{aligned} \tag{3}$$

determining the temperature field $T_1(\boldsymbol{x}, t)$ in the cladding region apart from the interface.

Due to the high heating rate in the ring region and the high thermal contact conductance (see table 1), a quasi-equilibrium temperature distribution is reached within few nanoseconds, as shown by the following estimation. The temporal heating behavior in the resonator ring is determined by the law of conservation of energy:

$$(\alpha I + \beta I^2)\pi Dbd = \rho_2 \pi Dbd c_{\mathrm{m2}} \partial_t T_2(t) + h_{12} \pi Db (T_2(t) - T_1(\boldsymbol{x}, t)|_{\mathrm{Interface}}). \tag{4}$$

Here, ρ_2 is the ring mass density, c_{m2} is the heat capacity and h_{12} is the thermal contact conductance. Further, πDbd is the ring volume and $T_1(\boldsymbol{x}, t)|_{\mathrm{Interface}}$ is the cladding temperature at the interface. Thus, the left side of equation (4) is the total absorbed power. That power is equal to the sum of the inserted heat in the ring per time and the heat flow through the interface per time, representing the right side. Considering a much slower heating rate in the large cladding, the solution of equation (4) is a saturating exponential increase of the ring temperature:

$$T_2(t) \approx T_1(\boldsymbol{x}, t)|_{\mathrm{Interface}} + d\,\frac{\alpha I + \beta I^2}{h_{12}}\left(1 - \exp\left[-\frac{h_{12}}{d\rho_2 c_{\mathrm{m2}}} t\right]\right). \tag{5}$$

For typical silicon ORR systems (see table 1), the corresponding heating time $t_{\mathrm{rise}} = d\rho_2 c_{\mathrm{m2}}/h_{12}$ is equal to 0.4 ns. Thus, the fast heating period in the ring region is neglected and a quasi-equilibrium temperature field $T_2(\boldsymbol{x}, t)$ is calculated, following the much slower heating process (µs-range, see figure 4) in the cladding. For that purpose, the cylindrical coordinate ϱ is shifted by $-D/2 + b/2$, resulting in a new radial coordinate $\tilde{\varrho} = \varrho - D/2 + b/2$. Due to the cylindrical symmetry, the problem is effectively two-dimensional with the waveguide cross-section $\widetilde{\Omega}_2 = [0, b] \times [0, d]$ as its rectangular domain. On the lower boundary $x_3 = 0$, a Dirichlet condition $T_{20}(\boldsymbol{x}, t)$ as well as a Neumann condition are enforced by the cladding temperature distribution $T_1(\boldsymbol{x}, t)|_{\mathrm{Interface}}$ and the thermal contact conductance at the interface [22]. On all other boundaries, exclusively insulating Neumann BCs are applied due to the air top cladding. The resulting mixed BC Poisson equation reads as

$$-\left(\partial_{\tilde{\varrho}}{}^2+\partial_{x_3}{}^2\right)T_2(\tilde{\boldsymbol{x}},t)=\frac{f_2}{a_2}\text{ in }\tilde{\Omega}_2,$$

$$T_2(\tilde{\boldsymbol{x}},t)|_{x_3=0}=T_{20}(\tilde{\boldsymbol{x}},t)\text{ and }\partial_{x_3}T_2(\tilde{\boldsymbol{x}},t)|_{x_3=0}=\frac{d}{\lambda_{\mathrm{Q2}}}(\alpha I+\beta I^2)\text{ and}$$

$$\partial_{\tilde{\varrho}}T_2(\tilde{\boldsymbol{x}},t)|_{\tilde{\varrho}=0}=\partial_{\tilde{\varrho}}T_2(\tilde{\boldsymbol{x}},t)|_{\tilde{\varrho}=b}=\partial_{x_3}T_2(\tilde{\boldsymbol{x}},t)|_{x_3=d}=0, \tag{6}$$

with the constant heat source

$$f_2=\frac{\alpha I+\beta I^2}{\rho_2 c_{\mathrm{m2}}}. \tag{7}$$

Solution for the temperature field

First, the bottom cladding temperature field $T_1(\boldsymbol{x},t)$ according to equation (3) is calculated. The solution of that boundary value problem is a convolution of the heat source $f_1(\boldsymbol{x},t)$ and a fundamental solution $G(\boldsymbol{x},\boldsymbol{x}',t)$ for the respective BCs [20]:

$$T_1(\boldsymbol{x},t)=T_0+\int_0^t\int_{\Omega_1}G(\boldsymbol{x},\boldsymbol{x}',t-t')f_1(\boldsymbol{x}')\mathrm{d}^3x'\mathrm{d}t'. \tag{8}$$

Here, the fundamental solution is the Greens function for the lower Euclidean half-space and insulating Neumann BCs:

$$G(\boldsymbol{x},\boldsymbol{x}',t)=\frac{1}{(4\pi a_1 t)^{\frac{3}{2}}}\left(\exp\left[-\frac{\|\boldsymbol{x}-\boldsymbol{x}'\|^2}{4a_1 t}\right]+\exp\left[-\frac{\|\boldsymbol{x}-\boldsymbol{x}'^*\|^2}{4a_1 t}\right]\right), \tag{9}$$

where $\boldsymbol{x}'^*\equiv(x_1',x_2',-x_3')$ is the reflection vector with respect to the x_1'-x_2'-plane. Due to $f_1(\boldsymbol{x})\propto\delta[x_3]$, see equation (2), exclusively values of G at $x_3'=0$ contribute to the convolution (8). Consequently, the distance in cylindrical coordinates fulfills $\|\boldsymbol{x}-\boldsymbol{x}'\|^2=\|\boldsymbol{x}-\boldsymbol{x}'^*\|^2=\varrho^2+\varrho'^2+x_3{}^2-2\varrho\varrho'\cos\varphi$ over the whole integration range. Using that distance in equation (8), the ϱ'- and x_3'-integration lead to

$$T_1(\boldsymbol{x},t)=T_0+Dbd\frac{\alpha I+\beta I^2}{\rho_1 c_{\mathrm{m1}}}\int_0^t\int_0^{2\pi}\frac{\exp\left[-\dfrac{\varrho^2+\left(\frac{D}{2}\right)^2+x_3{}^2-\varrho D\cos\varphi'}{4a_1(t-t')}\right]}{\left(4\pi a_1(t-t')\right)^{\frac{3}{2}}}\mathrm{d}\varphi'\mathrm{d}t'. \tag{10}$$

While the φ'-integral represents a hyperbolic Bessel function of first kind I_0 [23], the remaining time integral cannot be expressed by elementary functions:

$$T_1(\boldsymbol{x},t)=T_0+\frac{2}{\sqrt{\pi}}Dbd\frac{\alpha I+\beta I^2}{\rho_1 c_{\mathrm{m1}}}\int_0^t\frac{\exp\left[-\dfrac{\varrho^2+\left(\frac{D}{2}\right)^2+x_3{}^2}{4a_1(t-t')}\right]\mathrm{I}_0\left[\dfrac{\varrho D}{4a_1(t-t')}\right]}{\left(4a_1(t-t')\right)^{\frac{3}{2}}}\mathrm{d}t'\text{ in }\Omega_1\backslash\left\{\boldsymbol{x}|\varrho\in\left[\frac{D}{2}-\frac{b}{2},\frac{D}{2}+\frac{b}{2}\right]\right\}. \tag{11}$$

Thus, the temperature increase in the bottom cladding $\Delta T_1=T_1-T_0$ is proportional to the total absorbed power $(\alpha I+\beta I^2)\pi Dbd$ and anti-proportional to the thermal conductivity $\lambda_{\mathrm{Q1}}=\rho_1 c_{\mathrm{m1}}a_1$. It asymptotically reaches zero for large distances, i.e. $\lim_{\|\boldsymbol{x}\|\to\infty}\Delta T_1(\boldsymbol{x},t)=0$. In thermal equilibrium, i.e. $t\to\infty$, the cladding temperature field can be further simplified. For that purpose, the mathematical identity [24]

$$\int_0^\infty\frac{1}{t'^{3/2}}\exp\left[-\frac{C_1}{t'}\right]\mathrm{I}_0\left[\frac{C_2}{t'}\right]\mathrm{d}t'=\sqrt{\frac{2}{\pi C_2}}\Re\left(K\left[\frac{1}{2}\left(\frac{C_1}{C_2}+1\right)\right]\right) \tag{12}$$

is utilized, where $\Re$ denotes the real part of the complete elliptic integral of first kind K. Thus, the thermal equilibrium temperature distribution $T_1(\boldsymbol{x},\infty)$ reads as

$$T_1(\boldsymbol{x},\infty) = T_0 + \frac{Dbd}{\sqrt{2}\pi\lambda_{\mathrm{Q1}}}\frac{\alpha I+\beta I^2}{\sqrt{\varrho D}}\Re\left(K\left[\frac{1}{2}\left(1+\frac{\varrho^2+\left(\frac{D}{2}\right)^2+{x_3}^2}{\varrho D}\right)\right]\right) \text{ in } \Omega_1\setminus\left\{\boldsymbol{x}|\varrho\in\left[\frac{D}{2}-\frac{b}{2},\frac{D}{2}+\frac{b}{2}\right]\right\}. \tag{13}$$

Directly at the interface, an approximately homogeneous temperature distribution emerges:

$$T_1(\boldsymbol{x},t) = T_1(\boldsymbol{x},t)|_{\varrho=\frac{D}{2}+\frac{b}{2},\,x_3=0} \text{ in } \Omega_1\cap\left\{\boldsymbol{x}|\varrho\in\left[\frac{D}{2}-\frac{b}{2},\frac{D}{2}+\frac{b}{2}\right]\right\}. \tag{14}$$

In order to obtain the temperature field $T_2(\boldsymbol{x},t)$ in the resonator ring from equation (6), the lower boundary temperature $T_{20}(\boldsymbol{x},t)$ must be determined. For that purpose, an energy balance for the heat flow through the interface between ring and bottom cladding is formulated, considering a quasi-equilibrium distribution in the former one:

$$\pi Dbd(\alpha I+\beta I^2) = h_{12}\pi Db\left(T_{20}(\boldsymbol{x},t)-T_1(\boldsymbol{x},t)|_{x_3=0}\right). \tag{15}$$

Here, the left side is the total absorbed power. In thermal equilibrium, that inserted heat completely flows through the interface to the bottom cladding. The corresponding heat transfer per time is represented by the right side of equation (15). Hereby, $T_{20}(\boldsymbol{x},t)$ is determined by the bottom cladding temperature field $T_1(\boldsymbol{x},t)|_{x_3=0}$ according to equation (14). Applying the superposition principle, the general solution of (6) is the sum of a particular solution $T_{2\mathrm{p}}(\tilde{\boldsymbol{x}},t)$ of the inhomogeneous Poisson equation and the general solution $T_{2\mathrm{h}}(\tilde{\boldsymbol{x}},t)$ of the homogeneous Laplace equation [25]. A particular solution that fulfills all Neumann BCs is

$$T_{2\mathrm{p}}(\tilde{\boldsymbol{x}},t) = \frac{f_2}{2a_2}x_3(2d-x_3). \tag{16}$$

As $T_{2\mathrm{p}}(\tilde{\boldsymbol{x}},t)|_{x_3=0}=0$ holds at the interface here, the BCs for the Laplace problem of the homogeneous solution remain unchanged, except $\partial_{x_3}T_{2\mathrm{h}}(\tilde{\boldsymbol{x}},t)|_{x_3=0}=0$, compare equation (6). A product separation ansatz leads to eigenvalue problems for the radial and x_3-dependencies. The general homogeneous solution is a superposition of all eigenstates, expressed by the Fourier series [26]

$$T_{2\mathrm{h}}(\tilde{\boldsymbol{x}},t) = c_0(t)+\sum_{m=1}^{\infty}c_m(t)(e^{-k_m x_3}e^{2k_m d}+e^{k_m x_3})\cos(k_m\tilde{\varrho}),\, k_m=\frac{m\pi}{b}. \tag{17}$$

The constant Dirichlet condition at the interface enforces $c_0(t)=T_{20}(t)$, while all higher Fourier coefficients equal zero. Thus, the resulting temperature field within the ring resonator reads as

$$T_2(\boldsymbol{x},t) = \frac{\alpha I+\beta I^2}{2\lambda_{\mathrm{Q2}}}x_3(2d-x_3)+\frac{d}{h_{12}}(\alpha I+\beta I^2)+T_1(\boldsymbol{x},t)|_{\varrho=\frac{D-b}{2},\,x_3=0}. \tag{18}$$

Here, the first summand describes the parabolic temperature distribution in x_3-direction, the second summand is the temperature step at the interface and the third summand is the cladding temperature.

3. THE FINITE ELEMENT MODEL

For the numerical computation, the software Comsol Multiphysics [27] is utilized. Only thermal equilibrium temperature distributions, i.e. $t\to\infty$, are determined here. Since the ring is the primary heat source when driven at the resonance wavelength, we can simplify the computation by using axis symmetry. Hereby, the geometric model consists of the silicon ring waveguide with width b, height d and diameter D (see table 1). The ring is surrounded by two half-spheres, as illustrated in figure 2: one for the upper air cladding and the one for the SiO_x bottom cladding beneath the waveguide. These two half-spheres are limiting the optical computation, using scattering boundary conditions. Another spherical domain is added, that is used to simulate an infinite SiO_x substrate as heat sink by imposing an infinite-element-domain condition with a fixed temperature boundary of T_0. The width of this domain is equal to 10 % of the radius R_{clad} of the

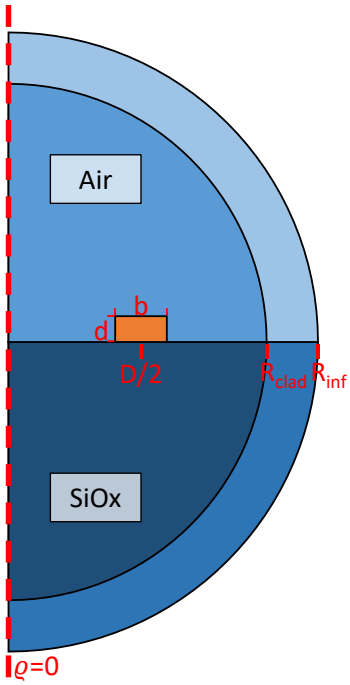

Figure 2. Sketch of the axis-symmetric model for the FEM computation. The inner sphere with radius R_{clad} marks the optical computation area. The outer sphere with radius R_{inf} utilizes the infinite-element-domain property to simulate an infinite SiO_x substrate with a fixed temperature of T_0.

entire system. The radius of both cladding domains is determined by sweeping the radius until the temperature of the ring waveguide converges to a constant value. This radius was found to be $R_{\mathrm{clad}} \approx 3 \cdot D$. Thermal radiation and convection at the air-solid-interfaces are neglected. A triangular mesh is used with a maximum element size of $\lambda/30$ within and $\lambda/12$ outside the waveguide core with a growth rate of 1.1. As a first simulation step, an eigenfrequency study is conducted to determine the exact optical resonance wavelength of the system, which is found to be at $\lambda = 1546.6\,\mathrm{nm}$. Afterwards, a user-defined port combined with a frequency-domain study is used to calculate the electromagnetic field distribution for several input powers. The intensity I within the ring is calculated from the electric field E as

$$I(\boldsymbol{x}) = \frac{1}{2} n_2 \varepsilon_0 c E(\boldsymbol{x})^2, \tag{19}$$

where n_2 is the refractive index of the ring, ε_0 is the vacuum permittivity and c is the vacuum speed of light. Cylindrical coordinates (ϱ, φ, x_3) are utilized. In thermal equilibrium, the time derivative in the heat equation vanishes, leading to

$$-a\boldsymbol{\nabla}^2 T(\boldsymbol{x}) = f(\boldsymbol{x}). \tag{20}$$

The heat source $f(\boldsymbol{x})$ is defined just like in equation (7), but with a spatially dependent intensity distribution $I(\boldsymbol{x})$ according to the electric field $E(\boldsymbol{x})$.

4. SELF-HEATING IN SILICON RESONATORS - RESULTS

Equations (11), (14) and (18) describe the spatially and time resolved temperature field in the whole ORR device analytically. The heating behavior is exemplarily calculated for a crystalline silicon resonator on silica glass with air as top cladding. All input parameters are summarized in table 1. This ORR was manufactured as part of a multi-project wafer run. Therefore, the geometric dimensions are the target design parameters without manufacturing design tolerances,

Table 1. Input parameters for the heating calculations.

Quantity	Symbol	Unit	Value	Source
diameter	D	nm	19130	design
width	b	nm	500	design
height	d	nm	220	design
thermal conductivity cladding (SiO_2)	λ_{Q1}	$\frac{W}{mK}$	1.3	[28]
thermal conductivity ring	λ_{Q2}	$\frac{W}{mK}$	130	[29]
linear attenuation coefficient	α	$\frac{1}{m}$	6.9	measured
TPA coefficient	β	$\frac{m}{W}$	8×10^{-12}	[30]
thermal contact conductance	h_{12}	$\frac{W}{m^2K}$	10^9	[31]
mass density cladding (SiO_2)	ρ_1	$\frac{kg}{m^3}$	2200	[32]
heat capacity cladding (SiO_2)	c_{m1}	$\frac{J}{kg\,K}$	1000	[33]
loss factor laser → chip	C_1	1	0.25	measured
coupling efficiency	C_2	1	0.01	simulated
Q-factor	Q	1	2.5×10^5	measured
free spectral range	FSR	nm	9.575	measured
full width at half maximum	$FWHM$	pm	7	measured
temperature sensitivity	$d\lambda/dT$	pm/K	68	[18]
operation wavelength	λ	nm	1546.6	measured

For a handy comparison between the measurable spectral shift $\Delta\lambda$ of the resonance and the calculated self-heating, both are determined as functions of the experimental accessible laser input power P_0 and wavelength sweep rate $d\lambda/dt$. The intensity I in the resonator is calculated as

$$I = C_1 C_2 Q \frac{FSR}{\lambda} \frac{P_0}{bd}, \tag{21}$$

where $C_1 C_2$ represents the portion of light from the laser that is coupled into the resonator ring, and $Q \times FSR/\lambda$ is the resonator finesse. Further, the excitation time t is determined by the $FWHM$ of the resonance and the wavelength sweep rate as

$$t = \frac{FWHM}{d\lambda/dt}. \tag{22}$$

Figure 3 shows the analytically calculated radial temperature distribution in the bottom cladding in thermal equilibrium according to equation (13), i.e. $\Delta T_1(\varrho, 0, \infty)$. An input laser power $P_0 = 0.4$ mW is utilized here, leading to a maximal heating amplitude of $\Delta T_1(D/2,0,\infty) \approx 19$ mK at the interface. For comparison, the FEM computed result is additionally depicted in figure 3 (b) (dashed line). The associated heating amplitude is with about 22.5 mK slightly higher than the analytically calculated one.

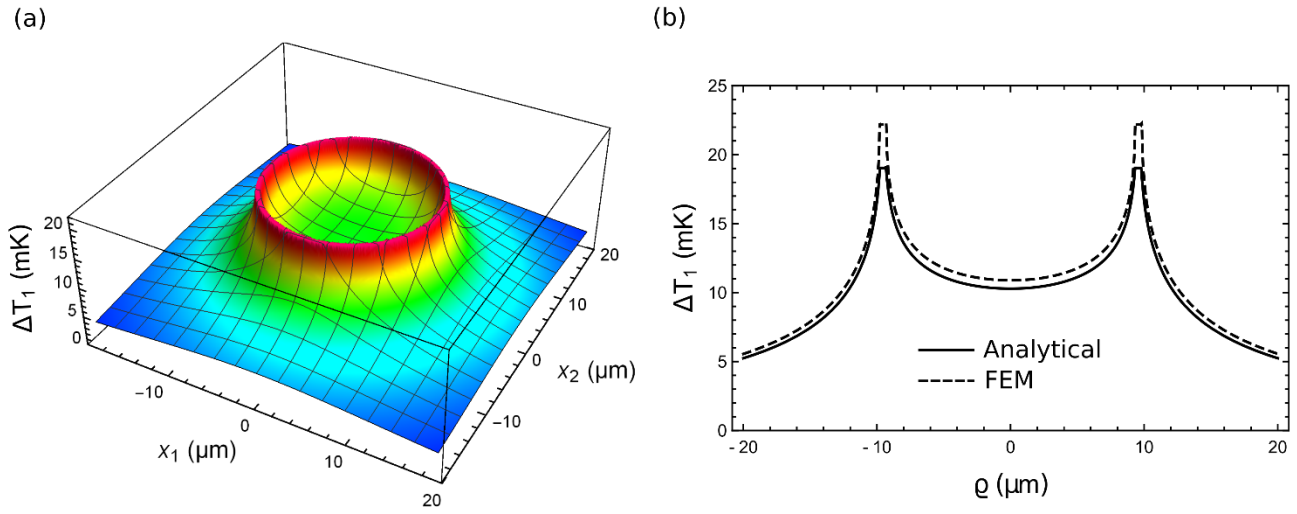

Figure 3. (a) Analytically calculated temperature field $\Delta T_1(x_1, x_2, 0, \infty)$ on the upper edge of the bottom cladding in thermal equilibrium. The input power P_0 is equal to 0.4 mW here. (b) Analytically calculated (solid line) and FEM computed (dashed line) radial temperature profile $\Delta T_1(\varrho, 0, \infty)$.

Figure 4 shows the analytically calculated resonator temperature increase as a function of time according to equation (18), i.e. $\Delta T_2(D/2,0,t)$. Additionally, the corresponding wavelength sweep rate and the resulting spectral resonance shift are depicted on the upper and on the right axis, respectively. Again, $P_0 = 0.4$ mW is utilized. It turns out that thermal response times of the ORR device under continuous wave excitation are in the µs-range: the excitation time for reaching half of the equilibrium temperature increase is $t_{0.5} \approx 13$ µs.

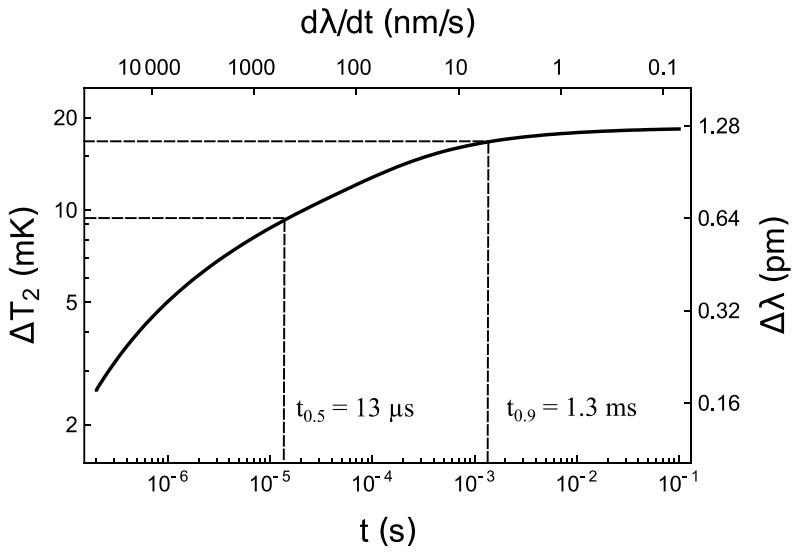

Figure 4. Analytically calculated temperature increase on the lower edge of the resonator ring $\Delta T_2(D/2,0,t)$. The input power P_0 is equal to 0.4 mW here.

Figure 5 shows the analytically calculated (solid lines) power dependence of the resonator temperature increase $\Delta T_2(D/2,0,t)$ for three different wavelength sweep rates according to equation (18). Again, the resulting spectral resonance shift is depicted on the right axis. Slower wavelength sweeping leads to a stronger heating effect, as the heating period gets longer. For relatively low excitation powers, i.e. $P_0 < P_{\mathrm{th}}$, linear absorption processes are the dominant heat source. Here, the temperature increase is proportional to the input power. For sufficiently high powers, i.e. $P_0 > P_{\mathrm{th}}$, TPA gets dominant and hence ΔT_2 rises quadratically with P_0. The threshold between those two regimes is calculated from the heat source (2) and intensity (21) to be $P_{\mathrm{th,ana}} \approx 22$ mW.

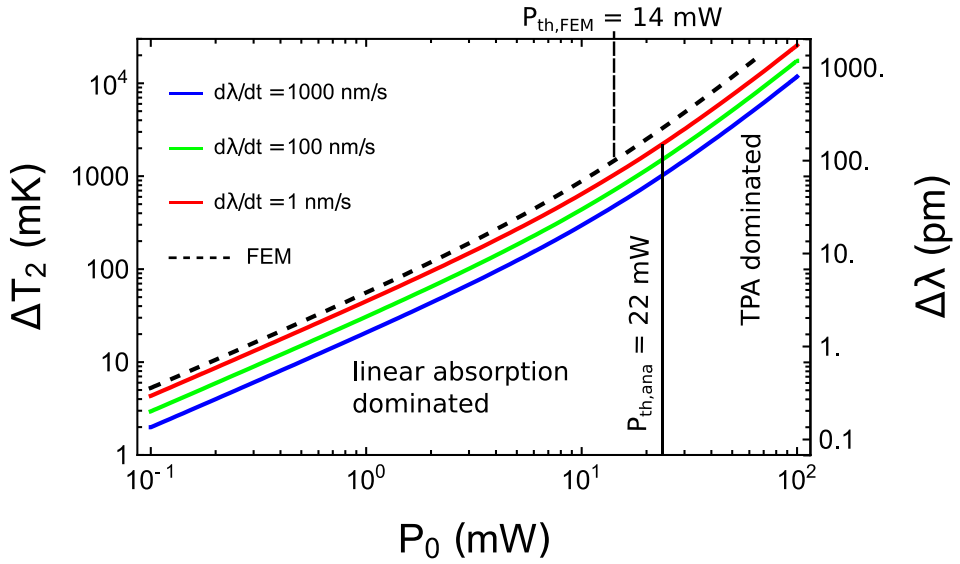

Figure 5. FEM computed (dashed line) and analytically calculated (solid lines) temperature increase on the lower edge of the resonator ring $\Delta T_2(D/2,0,t)$ as a function of input power P_0 for three different wavelength sweep rates $\mathrm{d}\lambda/\mathrm{d}t$.

For comparison, the respective FEM computed power dependence is depicted in figure 5 as well (dashed line). That simulation result is referring to thermal equilibrium, i.e. $\mathrm{d}\lambda/\mathrm{d}t \to 0$. As already shown in figure 3 (b), the simulated heating amplitude is slightly higher than the analytically calculated one in the linear regime. That deviation increases in the TPA dominated regime. Thus, the FEM computed threshold is with about $P_{\mathrm{th,FEM}} \approx 14$ mW significantly lower than $P_{\mathrm{th,ana}}$. The overestimation of P_{th} in our analytical model is a result of approximation (III) (see section 2.2): a homogeneous intensity distribution within the ring waveguide leads to lower peak intensities, and thus to a lower threshold. In general, P_{th} is determined by an equality of the total absorbed power due to linear and quadratic absorption:

$$\alpha \int_{\Omega_2} I_{\mathrm{th}}(\varrho, x_3)\,\mathrm{d}\varrho\mathrm{d}x_3 \equiv \beta \int_{\Omega_2} {I_{\mathrm{th}}}^2(\varrho, x_3)\,\mathrm{d}\varrho\mathrm{d}x_3 \text{ with } P_{\mathrm{th}} = \frac{FSR}{\lambda C_1 C_2 Q} \int_{\Omega_2} I_{\mathrm{th}}(\varrho, x_3)\,\mathrm{d}\varrho\mathrm{d}x_3. \tag{23}$$

The FEM computed electric field distribution $E(\varrho, x_3) \propto I^{1/2}(\varrho, x_3)$ is depicted in figure 6. Utilizing this simulation result, a homogeneous distribution for the analytical model and equation (23) leads to the ratio $P_{\mathrm{th,ana}}/P_{\mathrm{th,FEM}}$:

$$\frac{P_{\mathrm{th,ana}}}{P_{\mathrm{th,FEM}}} = \frac{bd \int_{\Omega_2} E^4(\varrho, x_3)\,\mathrm{d}\varrho\mathrm{d}x_3}{\left(\int_{\Omega_2} E^2(\varrho, x_3)\,\mathrm{d}\varrho\mathrm{d}x_3\right)^2} \approx 1.40. \tag{24}$$

The threshold between the linear absorption and the TPA dominated regimes marks an important transition in ORR systems, as optical bistability effects are caused by TPA [13-15].

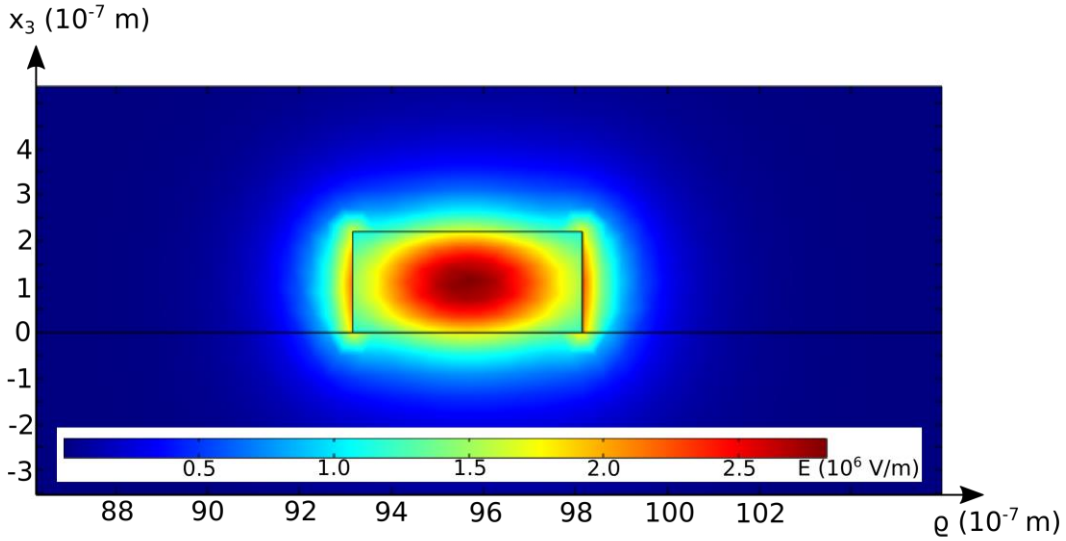

Figure 6. FEM computed electric field distribution $E(\varrho, x_3)$ on resonance within the resonator ring cross-section for an input power $P_0 = 0.4$ mW.

5. CONCLUSION AND OUTLOOK

In this work, we investigate the dynamical self-heating effect in optically excited optical microring resonators (ORRs). For that purpose, the heat equation boundary value problem under continuous excitation is solved in air cladded ORRs. We derive completely analytical expressions for the spatially and time dependent temperature fields. The self-heating effect is explicitly calculated for a widely applied ORR technology platform [9,34,35]: a silicon ring resonator on a silica glass bottom cladding. More explicitly, this ORR was produced using a multi-project wafer prototyping process. Experimentally determined parameters (see table 1) were included in the calculations. It is shown that the heating amplitude, which is about 50 mK for an input power of 1 mW, is mainly determined by the bottom cladding due to its small thermal conductivity. Excitation times for reaching half of the equilibrium temperature increase are in the range of a few µs, and therefore about 10^4 times larger than typical charge carrier lifetimes in the resonator ring [17]. As expected, the heating amplitude rises linearly with the input power in the linear absorption dominated and quadratically in the TPA dominated regime. In the latter power range (here above a threshold of about 14 mW), optical bistability effects cause significant asymmetries in the resonance shape [13-15].

The analytical results are verified by rigorous finite element simulations (FEM) in thermal equilibrium. For this purpose, the software Comsol Multiphysics [27] is utilized. Both analytical and numerical results are in good agreement down to a deviation of about 20 % in the heating amplitude and of about 55 % in the TPA threshold. Those deviations are due to a simplification in the analytical model, namely a homogeneous intensity distribution in the ring. The derived equations enable the determination of the whole temperature field with drastically reduced computational effort compared to FEM simulations, which enables fast scans over the whole parameter space. In future, the derived analytical model shall be extended by charge carrier dynamics and optical bistability effects. That extension would enable the modelling of absorption induced resonance distortions at low computational costs.

ACKNOWLEDGEMENT

This work is funded through the project 17FUN05 “PhotOQuant” within the Programme EMPIR. The EMPIR initiative is co-founded by the European Union’s Horizon 2020 research and innovation program and the EMPIR Participating Countries.

REFERENCES

[1] Sarkaleh, A. K., Lahijani, B. V., Saberkari, H. and Esmaeeli, A., "Optical ring resonators: a platform for biological sensing applications," Journal of Medical signals and sensors **7**(3), 185-191 (2017).
[2] Chao, C. Y. and Guo, L. J., "Design and optimization of microring resonators in biochemical sensing applications," Journal of lightwave technology 24(3), 1395-1402 (2006).
[3] Sun, Y. and Fan, X., "Optical ring resonators for biochemical and chemical sensing," Analytical and bioanalytical chemistry 399(1), 205-211 (2011).
[4] Sun, Y. and Fan, X., "Analysis of ring resonators for chemical vapor sensor development," Optics Express 16(14), 10254-10268 (2008).
[5] Campanella, C. E., De Leonardis, F., Mastronardi, L., Malara, P., Gagliardi, G. and Passaro, V. M., "Investigation of refractive index sensing based on Fano resonance in fiber Bragg grating ring resonators," Optics express 23(11), 14301-14313 (2015).
[6] Vollmer, F. and Fischer, P., "Frequency-domain displacement sensing with a fiber ring-resonator containing a variable gap," Sensors and Actuators A: Physical 134(2), 410-413 (2007).
[7] Kim, H. T. and Yu, M., "Cascaded ring resonator-based temperature sensor with simultaneously enhanced sensitivity and range," Optics Express 24(9), 9501-9510 (2016).
[8] Xu, H., Hafezi, M., Fan, J., Taylor, J. M., Strouse, G. F. and Ahmed, Z., "Ultra-sensitive chip-based photonic temperature sensor using ring resonator structures," Optics Express 22(3), 3098-3104 (2014).
[9] Bogaerts, W., De Heyn, P., Van Vaerenbergh, T., De Vos, K., Kumar Selvaraja, S., Claes, T., Dumon, P., Bienstman, P., Van Thourhout, D. and Baets, R., "Silicon microring resonators," Laser & Photonics Reviews 6(1), 47-73 (2012).
[10] Acharyya, N. and Kozyreff, G., "Multiple critical couplings and sensing in a microresonator-waveguide system," Physical Review Applied 8(3), 034029 (2017).
[11] Stern, F. and Dixon, J. R., "Narrowing the energy gap in semiconductors by compensation," Journal of Applied Physics 30(2), 268-269 (1959).
[12] Burstein, E., "Anomalous optical absorption limit in InSb," Physical review 93(3), 632 (1954).
[13] Gibbs, H. M., McCall, S. L., Venkatesan, T. N. C., Gossard, A. C., Passner, A. and Wiegmann, W., "Optical bistability in semiconductors," Applied Physics Letters 35(6), 451-453 (1979).
[14] Van Stryland, E. W., Woodall, M. A., Vanherzeele, H. and Soileau, M. J., "Energy band-gap dependence of two-photon absorption," Optics letters 10(10), 490-492 (1985).
[15] Rukhlenko, I. D., Premaratne, M. and Agrawal, G. P., "Analytical study of optical bistability in silicon ring resonators," Optics letters 35(1), 55-57 (2010).
[16] Hodgkinson, R. J., "Impact ionization and quantum efficiency in silicon," Proceedings of the Physical Society (1958-1967) 82(1), 58 (1963).
[17] Pernice, W. H., Li, M. and Tang, H. X., "Time-domain measurement of optical transport in silicon micro-ring resonators," Optics express 18(17), 18438-18452 (2010).
[18] Weituschat, L. M., Dickmann, W., Guimbao, J., Ramos, D., Kroker, S. and Postigo, P. A., "Photonic and thermal modelling of microrings in silicon, diamond and gan for temperature sensing," Nanomaterials 10(5), 934 (2020).
[19] Van, V., [Optical microring resonators: theory, techniques, and applications], CRC Press, 2-3 (2016).
[20] Barbu, V., [Partial differential equations and boundary value problems, Vol. 441], Springer Science & Business Media, 181-236 (2013).
[21] Bass, M., [Handbook of optics, Vol. 1], New York: McGraw-Hill Professional, 9.32. (1994).
[22] Pinsky, M. A., [Partial differential equations and boundary-value problems with applications, Vol. 15], American Mathematical Soc., 101 (2011).
[23] Dattoli, G. and Torre, A., [Theory and applications of generalized Bessel functions], Rome: Aracne, 23-25 (1996).
[24] Luke, Y. L., [Integrals of Bessel functions], Courier Corporation, 312-323 (2014).
[25] Pinsky, M. A., [Partial differential equations and boundary-value problems with applications, Vol. 15], American Mathematical Soc., 3 (2011).
[26] Pinsky, M. A., [Partial differential equations and boundary-value problems with applications, Vol. 15], American Mathematical Soc., 35 (2011).

[27] COMSOL AB, Stockholm, Sweden, "COMSOL Multiphysics® v. 5.3.," Slate, 07 September 2017, <www.comsol.com> (21 May 2021).
[28] Wray, K. L. and Connolly, T. J., "Thermal conductivity of clear fused silica at high temperatures," Journal of Applied Physics 30(11), 1702-1705 (1959).
[29] Slack, G. A., "Thermal conductivity of pure and impure silicon, silicon carbide, and diamond," Journal of Applied physics 35(12), 3460-3466 (1964).
[30] Dinu, M., Quochi, F. and Garcia, H., "Third-order nonlinearities in silicon at telecom wavelengths," Applied physics letters 82(18), 2954-2956 (2003).
[31] Chen, J., Zhang, G. and Li, B., "Thermal contact resistance across nanoscale silicon dioxide and silicon interface," Journal of Applied Physics 112(6), 064319 (2012).
[32] Bansal, N. P. and Doremus, R. H., [Handbook of glass properties], Elsevier, 54 (2013).
[33] Bansal, N. P. and Doremus, R. H., [Handbook of glass properties], Elsevier, 180 (2013).
[34] Nawrocka, M. S., Liu, T., Wang, X. and Panepucci, R. R., "Tunable silicon microring resonator with wide free spectral range," Applied physics letters 89(7), 071110 (2006).
[35] Turner, A. C., Foster, M. A., Gaeta, A. L. and Lipson, M., "Ultra-low power parametric frequency conversion in a silicon microring resonator," Optics express 16(7), 4881-4887 (2008).